J. Fluid Mech. (2020), *vol.* 890, A19. © The Author(s), 2020.
Published by Cambridge University Press
doi:10.1017/jfm.2020.120

Friction properties of superhydrophobic ridges

Hélène de Maleprade[1,2], Armelle Keiser[1,2], Christophe Clanet[1,2] and David Quéré[1,2,†]

[1]Physique and Mécanique des Milieux Hétérogènes, UMR 7636 du CNRS, ESPCI, PSL research University, 75005 Paris, France

[2]LadHyX, UMR 7646 du CNRS, École polytechnique, 91128 Palaiseau, France

(Received 10 September 2019; revised 21 January 2020; accepted 7 February 2020)

The extreme mobility of droplets on non-wetting materials implies the necessity of controlling their motion, direction or speed. In this paper, we show how ridges allow us to tune drop friction. Depending on the liquid speed and viscosity, two regimes emerge: fast drops with low viscosity dynamically deform and undergo inertial friction, so that their velocity is eventually fixed by the deformations induced by the ridges; in contrast, viscous drops hardly interact with the texture, so that their velocity is classically limited by viscous dissipation, as on a flat substrate. The transition between these two regimes reveals spectacular morphological changes: drops with intermediate viscosity elongate and adopt worm-like shapes, which we qualitatively describe.

Key words: drops, capillary flows

1. Introduction

From lotus leaves (Barthlott & Neinhuis 1997) to insects such as notonectae (Ditsche-Kuru *et al.* 2011), non-wetting materials are encountered in both the vegetal and animal kingdoms, and have inspired a wide range of applications such as cleaning (Blossey 2003; Solga *et al.* 2007), liquid transport (Rothstein 2010), underwater insulation (Calder 1969), breathing (Flynn & Bush 2008) and reduction of friction (Ybert *et al.* 2007). Specifically, water drops can reach velocities as high as a few m s^{-1} on tilted repellent materials (Olin *et al.* 2013; Mouterde *et al.* 2019), a consequence of an extremely low adhesion and friction (Hao *et al.* 2010). The reduction of water/substrate interactions is permitted by the nature of those surfaces that display a roughness (typically at a micrometric scale) made of hydrophobic materials (Wenzel 1936; Cassie & Baxter 1944). Since water (or water/glycerol solutions) only faces the top of the texture, it rests in a 'fakir' state that minimizes the actual contact with the solid (Johnson & Dettre 1964; de Gennes 1985). The robustness of the water repellence is conditioned by the stability of the air layer between the liquid and the substrate. Numerous studies have investigated criteria for this air-layer entrapment, as a function of texture design, wetting properties or pressure load from the liquid on the surface (Yang, Tartaglino & Persson 2006; Gross *et al.* 2010; Sheng & Zhang 2011; Carbone & Mangialardi 2015).

† Email address for correspondence: david.quere@espci.fr

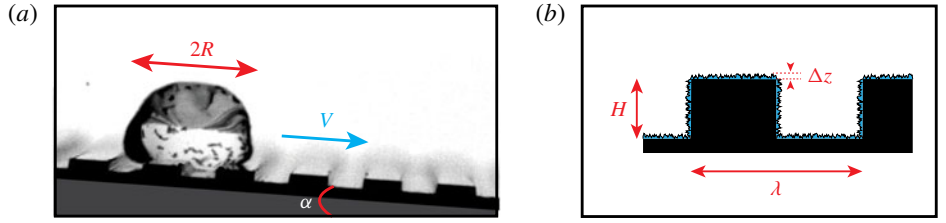

FIGURE 1. (*a*) Side view of the experiment: a drop with volume Ω and equatorial radius R runs down a superhydrophobic material macrotextured by ridges and tilted by an angle α. The terminal drop velocity is denoted as V. (*b*) The ridges, with depth H and wavelength λ, are uniformly covered by a microtexture that provides water repellency. The thickness Δz of this texture is typically 100 nm, much smaller than the ridge scale (between 100 μm and 1 mm).

In addition to the microscopic texture responsible for reinforced hydrophobicity, a macrotexture of same wettability can induce additional properties, often related to the dynamics of liquids. Macrotexture, at an intermediate scale between the microtexture and the drop size, will often have the ability to reshape water sitting or impacting on these materials. For instance, the contact time of a bouncing drop is strongly affected by the presence of a slender macrotexture that redistributes the mass of the liquid, which results in a shortening of the contact time by a factor often of order 2 (Bird *et al.* 2013). In the adjacent field of Leidenfrost drops, where levitation provided by the substrate temperature maximizes the mobility, ratchet-like macrotexture was found both to induce self-propulsion along the structure at the top surface of the solids (Linke *et al.* 2006) and to enhance the friction of water (Dupeux *et al.* 2011).

Inspired by these observations, we discuss here how ridges modify the friction of moving non-wetting liquids at room temperature, when placed perpendicular to the direction of the drops. The simplicity of our design was chosen to be characteristic of many liquid–obstacle interactions: as a liquid meets such ridges, it possibly deforms and its soft shock against the solid is a universal technique to slow down objects. We expect the macrotexture height and shape to provide a fine control of the friction, and thus of the velocity of the drops (Jiang & Li 2017). We show that superhydrophobic ridges can reduce the water mobility typically by one decade. We aim at understanding the specific friction under these conditions and develop to that end an extensive model of inertial friction where the role of drop deformation is investigated. We also consider the case of viscous liquids (Mahadevan & Pomeau 1999; Yariv & Schnitzer 2019), for which it is found that the effect of macrotexture is dramatically lowered. Surprisingly, intermediate viscosities reveal original effects, with spectacular drop elongations, which we qualitatively describe and comment on.

2. Experiments

In our experiments, non-wetting liquids run down superhydrophobic aluminium surfaces where ridges have been etched perpendicular to the direction of motion, as illustrated in figure 1. Ridges, with depths $H = 150$, 220, 350, 500, 700 and 1000 μm, have generally a wavelength $\lambda = 3$ mm equally shared between protrusions and indentations. The surfaces with total length ∼30 cm are rendered superhydrophobic by drawing them out of a solution of silanized silica nanobeads with diameter 30 nm (Glaco, Soft99). After solvent evaporation, the coating is consolidated at 250 °C

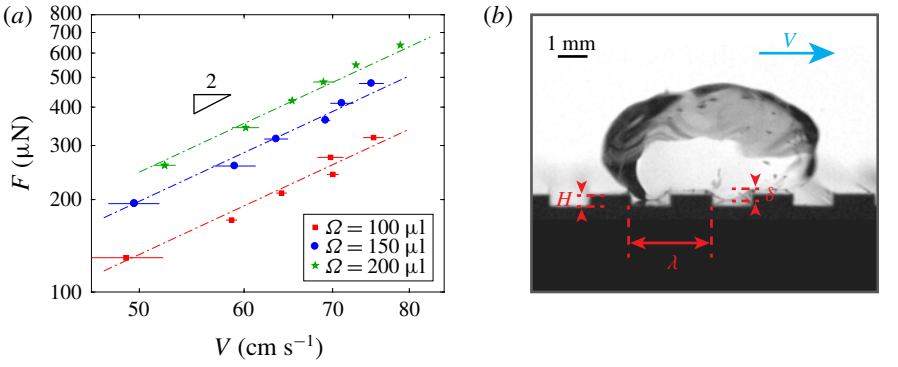

FIGURE 2. (*a*) Friction force F for water drops with volume $\Omega = 100$ µl (red square), $\Omega = 150$ µl (blue disc) and $\Omega = 200$ µl (green star) as a function of their terminal velocity V. Data are obtained by varying the substrate tilt α from 7° to 19°. Coloured lines all have a slope 2, as predicted by (3.1). (*b*) Water drop ($\Omega = 100$ µl) on superhydrophobic ridges with $H = 350$ µm and $\lambda = 3$ mm. The drop weight generates bulges with depth δ.

for 30 min. To ensure nanoparticle coverage over the whole surface, especially at corners, the process is repeated three times and the resulting coating exhibits a typical roughness of 100 nm, as shown by atomic force microscopy. A similar treatment on a flat material leads to advancing and receding contact angles for water $\theta_a = 171 \pm 2°$ and $\theta_r = 165 \pm 2°$, two values typical of a superhydrophobic material.

Then, we place a drop of a water/glycerol mixture (density ρ, viscosity η and surface tension γ) on the ridged solid. Drops have a volume $\Omega = 100$–200 µl, so that on a horizontal surface and at rest, their equatorial radius R is larger than the capillary length $a = \sqrt{\gamma/\rho g}$, where g is the acceleration due to gravity. In the following, we refer to this value as the radius R, despite the complicated shapes sometimes adopted by the liquid. These drops are flattened by gravity, and they have a thickness $\sim 2a$ and a volume $\Omega \approx 2\pi R^2 a$. As we tilt the substrate by an angle α (figure 1), we first observe that a non-zero angle α^* is needed for drops to depart ($\alpha^* = 3 \pm 1°$ for $\Omega = 100$ µl), a consequence of their (small) adhesion and deformation in the ridges. The tilt angle α in our experiments ranges from 10° to 17° ($\alpha \gg \alpha^*$), allowing us to neglect the small liquid adhesion in what follows. In such conditions, we follow the drop velocity at all times using a video-camera Optronis CR600x2 shooting at 300 f.p.s. The drop velocity first increases and it rapidly reaches a plateau value V, which we measure. The friction being known (it simply balances the weight $\rho\Omega g\alpha$ in this plateau regime), our experiment simply allows us to access the relationship between resistance and velocity, a crucial information to understand the nature of the friction. We aim here at describing how ridges influence the speed, which we analyse by varying drop volume, texture parameters and liquid viscosity. We first present results for water, and then increase the viscosity by using water/glycerol mixtures.

3. Inertial friction

As seen in figure 2(*a*), water on tilted ridges move at a few tens of cm s^{-1}, that is, approximately 10 times slower than on flat superhydrophobic substrates (Olin *et al.*

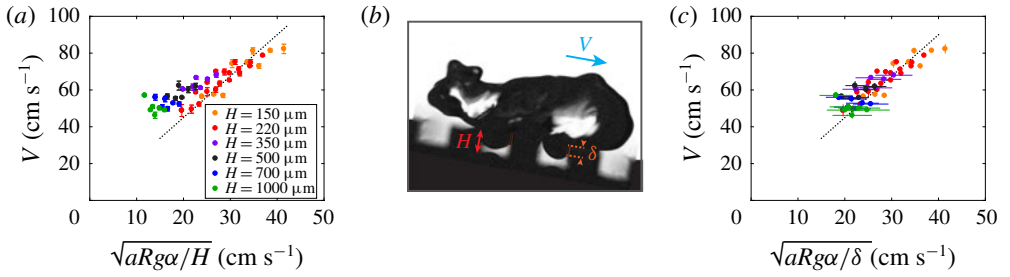

FIGURE 3. (*a*) Drop terminal velocity V as a function of its theoretical expression (3.2). Colours indicate the ridge depth: $H = 150$ μm (orange), $H = 220$ μm (red), $H = 350$ μm (purple), $H = 500$ μm (black), $H = 700$ μm (blue) and $H = 1000$ μm (green). The line shows equation (3.2) with a prefactor of 2.3. (*b*) Water with volume $\Omega = 100$ μl moving on deep ridges ($H = 1000$ μm) tilted by $\alpha = 10.5°$. The bulge amplitude δ is smaller than H. (*c*) Drop terminal velocity V as a function of the value predicted by (3.2) where H is replaced by the measured δ, $V = [aRg\alpha/\delta]^{1/2}$, drawn with a prefactor of 2.3. Symbols are the same as in (*a*).

2013; Mouterde *et al.* 2019). Hence friction is markedly enhanced by the presence of ridges. The Reynolds number $Re = \rho VR/\eta$ is typically 10^3, which suggests an inertial kind of friction, that is, quadratic in velocity. Indeed, the friction force F in figure 2(*a*) is observed to vary as the square of the terminal velocity V (slope 2 in this logarithmic plot), whatever the drop volume. Figures 1 and 2(*b*) also reveal that ridges generate bulges with amplitude δ at the drop base. As shown by Dupeux *et al.*, such bulges are also observed for Leidenfrost drops moving on ridges, and these authors assumed that their soft shocks on protrusions enhance friction (Dupeux *et al.* 2011). The volume of a bulge scaling as $\delta\lambda R$, the typical loss of kinetic energy per bulge is $\rho\delta\lambda RV^2$, which leads to an inertial friction force scaling as V^2 – and thus particularly efficient for slowing down the quick drops generally observed in non-wetting situations.

We show how this first model must be adapted to account for our observations. For the sake of simplicity, we start by considering grooves fully filled by water (δ=H). As a bulge (whose volume scales as $H\lambda R$) penetrates an indentation, it remains trapped until the rest of water has passed above, so that the corresponding loss in kinetic energy only happens in the front groove. This differs from the Dupeux model, where dissipation was assumed to be proportional to the number of ridges below the drop. Hence, we expect an energy loss scaling as $\rho H\lambda RV^2$ per newly explored ridge. This quantity can be seen as the work λF_1 of a friction force F_1 over the wavelength λ, which yields

$$F_1 \approx \rho HRV^2. \tag{3.1}$$

This friction is quadratic in velocity, as observed in experiments (figure 2*a*). Balancing it with the driving force $\rho R^2 ag\alpha$ leads to an expression for the terminal velocity

$$V \approx [aRg\alpha/H]^{1/2}. \tag{3.2}$$

Experimental results are compared to this prediction in figure 3(*a*). Data collapse on a straight line passing through the origin when ridges are shallow ($H = 150$ μm, orange data; $H = 220$ μm, red data). For deeper indentations, motion is quicker than predicted (by up to 50 % for $H = 1000$ μm), which indicates that the model then overestimates friction.

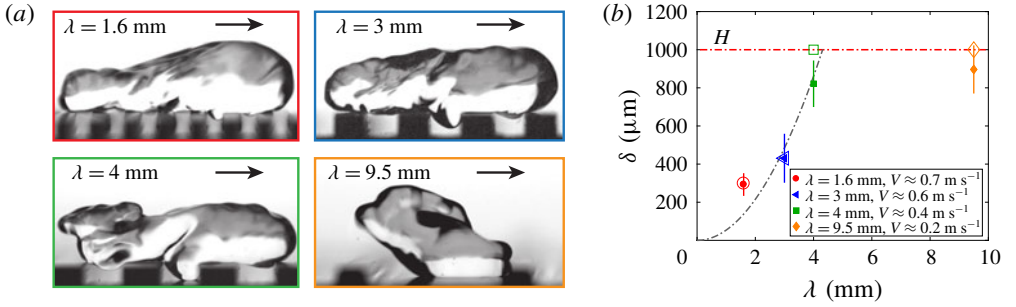

FIGURE 4. (*a*) Water drops ($\Omega = 100$ μl) moving on superhydrophobic ridges ($\alpha = 12°$, $H = 1000$ μm) for $\lambda = 1.6$ mm (red), $\lambda = 3$ mm (blue), $\lambda = 4$ mm (green) and $\lambda = 9.5$ mm (groove width 8 mm, wall thickness 1.5 mm, orange). (*b*) Size δ of the water bulge, as a function of the ridge wavelength λ, for the droplets in (*a*). Filled and hollow symbols respectively show data and predictions from (3.3). The grey dashed line shows (3.3) at the average velocity of the experiments, until saturation once δ reaches the indentation height $H = 1000$ μm.

As seen in figure 3(*b*) and in the supplemental movie 1 available at https://doi.org/10.1017/jfm.2020.120, side views reveal that water does not fill deep grooves. For bulges with $\delta < H$, equation (3.1) has to be modified into $F \approx \rho\delta RV^2$, which yields $V \approx [aRg\alpha/\delta]^{1/2}$ – a velocity larger than predicted by (3.2). The bulge depth δ can be estimated from photos such as in figure 3(*b*), which allows us to compare the latter prediction with observations (figure 3*c*). The dynamical character of δ scatters the data (horizontal bars in the figure), but we get a satisfactory collapse of the whole set of experiments along a straight line passing through the origin. The prefactor used for fitting the data is 2.3 ± 0.2, in good agreement with the value $\sqrt{2\pi} \approx 2.5$ expected if taking into account the numerical coefficient of the drop volume Ω in the model.

However, this approach remains semi-empirical, which we can improve by discussing the value of δ. To that end, we first look at the influence of the ridge wavelength λ for $H = 1000$ μm and $\alpha = 12°$. As seen in figure 4(*a*), the bulge thickness δ logically tends to vanish at small λ (water hardly penetrates narrow ridges). More generally, we report in figure 4(*b*) how δ increases with λ and saturates ($\delta = H$) at large λ. Note that the point for $\lambda = 9.5$ mm is the only one in the study where the indentation width (8 mm) is not equal to the protrusion width (1.5 mm).

The depth δ_o of a static bulge can be described by balancing surface tension and gravity. A bulge is modelled by a spherical cap with radius $\lambda/4$ inside the indentation, and its radius of curvature scales as $2\delta_o/(\lambda/4)^2$. Balancing the corresponding Laplace pressure $2\gamma\delta/(\lambda/4)^2$ by the hydrostatic pressure $2\rho ga$ yields $\delta_o \approx \lambda^2/16a$. This depth can be amplified by motion: as it hits the protrusion side at a velocity of order V, a bulge is entrained by inertia within the indentation. If we express that the bulge depth results from a balance between Laplace and dynamical pressure $\rho V^2/2$, we obtain

$$\delta \sim \delta_o \left(\frac{V}{V^*}\right)^2, \tag{3.3}$$

where the characteristic gravitational speed $V^* = 2\sqrt{ga}$ is 30 cm s^{-1}. Equation (3.3) shows that the bulges are amplified by the liquid velocity, but this also has natural

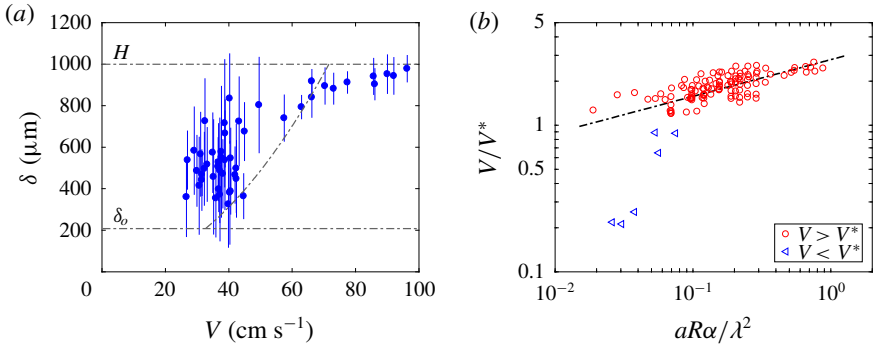

FIGURE 5. (*a*) Bulge depth δ as a function of the water drop velocity V on ridges with $H = 1000$ μm and $\lambda = 3$ mm, for $\Omega = 100$ μl and $\alpha = 12°$. Dashed lines successively show the static value $\delta_o \approx \lambda^2/16a$ ($V < V^* \approx 30$ cm s^{-1}), equation (3.3) and saturation ($\delta = H$). (*b*) Dimensionless velocity V/V^* as a function of the geometrical number $aR\alpha/\lambda^2$. The dashed line has the slope 1/4 predicted by (3.4). Red circles and blue triangles respectively stand for data with $V > V^*$ and $V < V^*$. Drop size R, indentation depth H, wavelength λ and tilt α are all varied in this experiment.

limits: (i) For $V < V^*$, the bulge depth δ is fixed by its minimum static value δ_o. (ii) At large speed, δ cannot diverge, being limited by the indentation depth; it saturates at $\delta = H$ for $V \approx 4V^*(Ha)^{1/2}/\lambda$ (typically 70 cm s^{-1} for $H = 1$ mm). Conversely, saturation at fixed V occurs when the ridge wavelength is larger than $\lambda^* \approx 4(Ha)^{1/2}V^*/V$. For $V \approx 50$ cm s^{-1}, λ^* is expected to be 4 mm, as observed in figure 4(*b*). If we calculate for each data point the deformation expected from (3.3) (empty symbols in figure 4*b*), we find a good accord with the observations. However, the deformation in the saturation region is slightly smaller than H, which might arise from the residual curvature of the bulge inside the (superhydrophobic) corners, preventing a shock over the full depth.

The bulge depth can also be measured as a function of the drop velocity V. To that end, we first exploit the regime of acceleration where V continuously varies at fixed tilt α and volume Ω. But we also can use a superhydrophobic track upstream from the ridges so that quick drops entering the ridged region decelerate against the protrusions, at fixed α and Ω. As seen in figure 5, water fully penetrates indentations ($\delta \approx H = 1000$ μm) at high V, which confirms that bulges grow with speed. For $V <$ 60 cm s^{-1}, data become scattered (due to oscillations at interfaces), but they indicate a decrease of δ down to the value where the bulge has no dynamical deformation ($V < V^* \approx 30$ cm s^{-1}) and reaches its static depth $\delta_o \approx \lambda^2/16a \approx 200$ μm.

The dynamical nature of the bulges explains the counterintuitive dependency of V on λ at large H. At first sight, we expect fewer shocks for wider ridges, and thus a smaller friction and a higher velocity. However, if we combine equations (3.2) and (3.3), we obtain a slowly decreasing function for the terminal velocity as a function of the ridge wavelength λ

$$V \approx V^* \left[\frac{aR}{\lambda^2}\alpha\right]^{1/4}. \tag{3.4}$$

We find that the drop velocity only increases as $\alpha^{1/4}$, in a less trivial way than if balancing inertial friction (in V^2) with gravity (in α). As discussed earlier, increasing the tilt makes drops sink into the texture, which amplifies friction and eventually

makes the velocity smaller than expected from a naïve argument. Water is also found to move slower on wide ridges ($V \sim \lambda^{-1/2}$), due again to the filling of cavities. In the opposite limit ($\lambda \to 0$), the repellent surface tends to behave as a flat surface of higher mobility. More generally, equation (3.4) is an explicit formula for the water velocity in deep repellent indentations with $\delta < H$, and it can be tested by gathering all our data. By plotting the dimensionless velocity V/V^* as a function of the number $aR\alpha/\lambda^2$ in figure 5(*b*), we observe that the large collection of data obtained by varying H, λ, α and R collapses along a line with slope 1/4 (drawn in black), in agreement with the scaling law in (3.4). The model is valid provided the drop velocity V is larger than V^*, and all the red data indeed satisfy this criterion. Conversely, the few data at $V < V^*$ and reported with blue symbols are found to largely deviate from the model, as expected in a situation where the bulge depth is simply given by its static value δ_0.

4. Viscous friction

After discussing the friction enhancement of water on ridges, we now come to more viscous water/glycerol mixtures (50 mPa s $< \eta <$ 1000 mPa s). The experiment is the same as in figure 1 and glycerol slightly increases the receding contact angle on a given repellent material: we measure an angle $\alpha^* = 4 \pm 1^\circ$ for drop departure (with $\Omega = 100$ µl), slightly larger than that with water $\alpha^* = 3 \pm 1^\circ$. All our tilts are anyway significantly larger than α^*, so that we can neglect this small variation.

A typical sequence is presented in figure 6(*a*) and supplemental movie 2, for a drop with $\eta = 500$ mPa s running down tilted ridges, the camera being inclined by the same angle $\alpha = 11.5^\circ$. After a short regime of acceleration, the drop reaches a plateau velocity V of a few cm s^{-1}, 10 times slower than water. Tracers at the surface show that the liquid hardly penetrates the indentations but rather rolls on their tops, as if the solid were flat (Mahadevan & Pomeau 1999; Yariv & Schnitzer 2019). The Reynolds number is typically $Re \approx 0.1$, which now suggests a friction of viscous origin. This can be checked by plotting the driving force $\rho\Omega g\alpha$ as a function of V, as done in figure 6(*b*) where we observe linear relationships between F and V (at all volumes), as generally expected for a viscous friction. Deviations observed at small velocity arise from contact angle hysteresis, which adds a resisting force at low speed.

The friction F of viscous liquid pearls was first discussed in a classical paper by Mahadevan & Pomeau (1999). At low Reynolds numbers, drops roll so that the viscous dissipation only takes place in the region flattened by gravity, in the vicinity of the solid substrate. The size of this region is quadratically sensitive to the radius R for drops smaller than the capillary length a, which generates a pathological behaviour, where pearls are found to be all the quicker since they are smaller. For puddles (our case), the physics is more usual: velocity gradients take place through the puddle thickness $\sim a$, so that integrating the viscous stress $\eta V/a$ over a surface area $\sim R^2$ provides a friction F scaling as $\eta V R^2/a$, that is, as $\eta V\Omega/a^2$. Therefore, F is linear in velocity V, with a coefficient of proportionality expected to be typically 2.5 g s^{-1} for $\Omega = 100$ µl. These findings agree with figure 6(*b*), where the coefficient is 4.5 g s^{-1} for $\Omega = 100$ µl and proportional to Ω for other volumes. Balancing F by gravity, we get

$$V \approx \gamma\alpha/\eta. \tag{4.1}$$

The velocity linearly depends on the tilt, the only parameter remaining from gravity. It is also inversely proportional to the viscosity η, a common feature at small Reynolds number. The graph 6(*c*) shows that equation (4.1) fairly describes our data. The dashed line with slope 1 is adjusted by a numerical coefficient of 0.4, close to unity and in

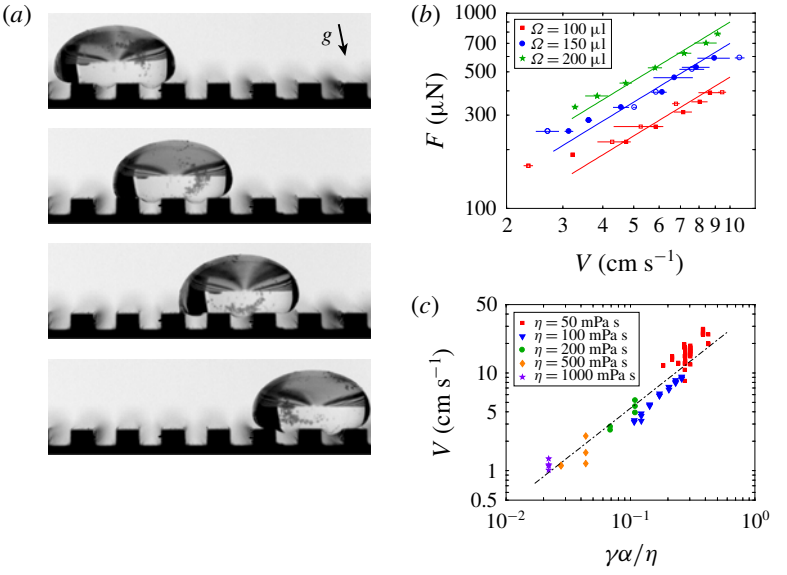

FIGURE 6. (*a*) Viscous drop (volume $\Omega = 100$ µl, viscosity $\eta = 500$ mPa s) moving on superhydrophobic ridges ($H = 1$ mm and $\lambda = 3$ mm) tilted by $\alpha = 11.5°$. Images are spaced by 0.2 s and tracers (diameter of 100 µm) highlight the rotation of the liquid. (*b*) Friction force F as a function of the terminal velocity V for drops with viscosity $\eta = 100$ mPa s and $\Omega = 100$ µl (red squares), $\Omega = 150$ µl (blue discs) and $\Omega = 200$ µl (green stars). Filled and hollow symbols respectively hold for $H = 220$ µm and $H = 350$ µm, at fixed $\lambda = 3$ mm. Lines have a slope 1, in agreement with our model. (*c*) Terminal velocity V as a function of its theoretical expression (4.1) for $\eta = 50$ mPa s (red squares), $\eta = 100$ mPa s (blue triangles), $\eta = 200$ mPa s (green discs), $\eta = 500$ mPa s (orange diamonds) and $\eta = 1000$ mPa s (purple stars). Equation (4.1) with a prefactor of 0.4 is shown with a dashed line.

excellent agreement with the fitting parameters in figure 6(*b*). The terminal velocity of viscous drops never exceeds 20 cm s^{-1}, below the characteristic speed $V^* \approx 30$ cm s^{-1} above which we expect dynamical bulges. This explains the absence of significant deformation in figure 6(*a*), where bulges simply show the static deformation $\delta_o \approx$ 200 µm: drops in the viscous regime keep a quasi-static shape as they move.

5. Transition from viscous to inertial behaviour

Up to now, we have considered asymptotic cases, where friction was either inertial or viscous. We now investigate what happens for liquids with intermediate viscosities ranging from 2 mPa s to 40 mPa s. Our main observation is reported in figure 7(*a*) (see also supplemental movies 3–7). It is found that drops in this regime abruptly (and spectacularly) elongate around $\eta \approx 3$ mPa s, before gradually shortening at larger viscosity and recovering a quasi-static shape for $\eta > 40$ mPa s, as discussed in the previous section. All drops having the same volume ($\Omega = 100$ µl), the elongation is accompanied by a thinning in the two other directions; however, the bump at the bottom interface remains localized in the first cavity met by the moving liquid, as discussed in § 3.

Observations can be made more quantitative by plotting the drop velocity V and length L as a function of η, at fixed other parameters (figure 7*b*). At low η

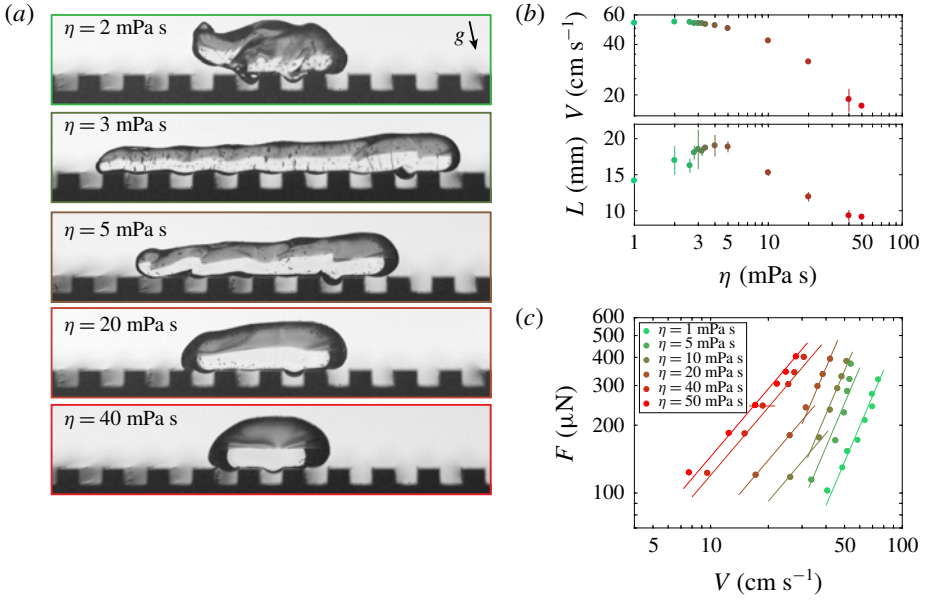

FIGURE 7. (*a*) Drops with intermediate viscosities ($\eta = 2$, 3, 5, 20 and 40 mPa s) moving on superhydrophobic ridges ($H = 1$ mm and $\lambda = 3$ mm) tilted by $\alpha = 12°$. The drop volume is $\Omega = 100$ µl. (*b*) Drop velocity V and terminal length L as a function of η, for $\Omega = 100$ µl, $\alpha = 12°$, $H = 1$ mm and $\lambda = 3$ mm. (*c*) Friction F as a function of V for $\Omega = 100$ µl, $H = 1$ mm, $\lambda = 3$ mm and various viscosities (same colour code as in *b*). Lines have successive slopes of 1 and 2, as respectively discussed in §§ 3 and 4.

(green points), V reaches its maximum, around 60 cm s^{-1}, and data plateau – a signature of inertial friction (§ 3). However, an increase of η (together with a small decrease of surface tension due to glycerol) can trigger the deposition of the liquid on the substrate (Landau–Levich transition) (Podgorski, Flesselles & Limat 2001), a phenomenon shown by Voinov and Cox to occur critically at a well-defined velocity depending on the surface tension, viscosity and contact angle (Voinov 1976; Cox 1986). The capillary number $Ca = \eta V/\gamma$ at which the transition takes place is typically between 0.01 and 0.1 (Podgorski *et al.* 2001), as observed in our experiment, where elongation critically appears around $Ca \approx 0.03$. However, the length L in figure 7(*b*) does not fully diverge, due to the action of surface tension that makes the liquid dewet from its end as soon as deposited, which limits the length of the slug.

As viscosity increases further, drops gradually recover their usual globular shape. We simultaneously notice the disappearance of waves at the surface, confirming the increasing role of viscosity. We gradually recover the viscous regime described in § 4, where the velocity V simply decreases as $1/\eta$, as indeed observed in figure 6(*c*) for $\eta > \sim 10$ mPa s. In this regime, the liquid does not slide anymore on the protrusions but rather rotates, which prevents deposition and explains that the drop shape can become quasi-static at a capillary number set by (4.1) to be $Ca = \alpha$, a value much smaller than unity.

We can also detect the transition from inertial to viscous regimes by looking at the friction F as a function of the terminal velocity V. Plotted in logarithmic scales for a large range of viscosities, the curves $F(V)$ are found in figure 7(*c*) to align with a slope 2 at small η and with a slope 1 at large η – the transition being observed

around $\eta = 10$–20 mPa s, values around which data obey these two scalings in V. The Reynolds number at the transition seems too large (approximately 10) if we calculate it with its usual expression $Re = \rho RV/\eta$. However, the inertial friction on ridges was shown to be $F = \rho\delta RV^2$, which generates a Reynolds number $Re = \rho\delta V/\eta$ indeed of order unity at the transition.

6. Conclusion

We described in this paper the specific friction arising from the presence of ridges on repellent materials. For water, of low viscosity, such obstacles have a main influence and are found to cut down the velocity. We studied how drops interact with the texture and how bulges form and dissipate energy as they impact the protrusion sides. In contrast, water/glycerol mixtures are too slow to dissipate energy in shocks and the velocity is classically fixed by a viscous friction. The transition from inertial to viscous regimes was found to imply spectacular drop elongations in a narrow window of liquid viscosity. Further work in this area could discuss the adhesion of water and viscous liquids on such ridges, whose shape might influence the pinning of liquids. A quantitative understanding of the drop elongation at intermediate viscosity would also be worth deriving. Moreover, all the results presented here are based on symmetrical ridges and we could wonder what happens if the textures turn asymmetrical, a relevant case in the context of self-propelling drops on ratchets.

Acknowledgements

We thank G. Dupeux and M.-C. Nguyen for preliminary experiments and discussions.

Declaration of interests

The authors report no conflict of interest.

Supplementary movies and material

Supplementary movies and material are available at https://doi.org/10.1017/jfm.2020.120.

REFERENCES

BARTHLOTT, W. & NEINHUIS, C. 1997 Purity of the sacred lotus, or escape from contamination in biological surfaces. *Planta* **202**, 1–8.

BIRD, J. C., DHIMAN, R., KWON, H.-M. & VARANASI, K. K. 2013 Reducing the contact time of a bouncing drop. *Nature* **503**, 385–388.

BLOSSEY, R. 2003 Self-cleaning surfaces – virtual realities. *Nat. Mater.* **2**, 301–306.

CALDER, W. A. 1969 Temperature relations and underwater endurance of the smallest homeothermic diver, the water shrew. *Compar. Biochem. Phys.* **30**, 1075–1082.

CARBONE, G. & MANGIALARDI, L. 2015 Hydrophobic properties of a wavy rough substrate. *Eur. Phys. J.* E **16**, 67–76.

CASSIE, A. B. D. & BAXTER, S. 1944 Wettability of porous surfaces. *Trans. Faraday Soc.* **40**, 546–551.

COX, R. G. 1986 The dynamics of the spreading of liquids on a solid surface. Part 1: viscous flow. *J. Fluid Mech.* **168**, 169–194.

DITSCHE-KURU, P., SCHNEIDER, E. S., MELSKOTTE, J. E., BREDE, M., LEDER, A. & BARTHLOTT, W. 2011 Superhydrophobic surfaces of the water bug notonecta glauca: a model for friction reduction and air retention. *Beilstein J. Nanotechnology* **2**, 137–144.

DUPEUX, G., LE MERRER, M., CLANET, C. & QUERE, D. 2011 Trapping Leidenfrost drops with crenelations. *Phys. Rev. Lett.* **107**, 114503.

FLYNN, M. R. & BUSH, J. W. M. 2008 Underwater breathing: the mechanics of plastron respiration. *J. Fluid Mech.* **608**, 275–296.

DE GENNES, P. G. 1985 Wetting: statics and dynamics. *Rev. Mod. Phys.* **57**, 827–863.

GROSS, M., VARNIK, F., RAABE, D. & STEINBACH, I. 2010 Small droplets on superhydrophobic substrates. *Phys. Rev.* E **81**, 051606.

HAO, P., LV, C., YAO, Z. & HE, F. 2010 Sliding behavior of water droplet on superhydrophobic surface. *Europhys. Lett.* **90**, 66003.

JIANG, X. & LI, H. Z. 2017 Liquid drops hurdling barriers of various geometries. *Adv. Mater. Interfaces* **4**, 1700516.

JOHNSON, R. E. & DETTRE, R. H. 1964 Contact angle, wettability and adhesion. *Adv. Chem. Ser.* **43**, 112–135.

LINKE, H., ALEMÁN, B. J., MELLING, L. D., TAORMINA, M. J., FRANCIS, M. J., DOW-HYGELUND, C. C., NARAYANAN, V., TAYLOR, R. P. & STOUT, A. 2006 Self-propelled Leidenfrost droplets. *Phys. Rev. Lett.* **96**, 154502.

MAHADEVAN, L. & POMEAU, Y. 1999 Rolling droplets. *Phys. Fluids* **11**, 2449–2453.

MOUTERDE, T., RAUX, P. S., CLANET, C. & QUERE, D. 2019 Superhydrophobic frictions. *Proc. Natl Acad. Sci. USA* **116**, 8220–8223.

OLIN, P. H., LINDSTRÖM, S. B., PETTERSSON, T. & WÅGBERG, L. 2013 Water drop friction on superhydrophobic surfaces. *Langmuir* **29**, 9079–9089.

PODGORSKI, T., FLESSELLES, J.-M. & LIMAT, L. 2001 Corners, cusps, and pearls in running drops. *Phys. Rev. Lett.* **87**, 036102.

ROTHSTEIN, J. P. 2010 Slip on superhydrophobic surfaces. *Annu. Rev. Fluid Mech.* **42**, 89–109.

SHENG, X. & ZHANG, J. 2011 Air layer on superhydrophobic surface underwater. *Colloids Surf.* A **377**, 374–378.

SOLGA, A., CERMAN, Z., STRIFFLER, B. F., SPAETH, M. & BARTHLOTT, W. 2007 The dream of staying clean: lotus and biomimetic surfaces. *Bioinspir. Biomim.* **2**, S126–S134.

VOINOV, O. V. 1976 Hydrodynamics of wetting. *Fluid Dyn.* **11**, 714–721.

WENZEL, R. N. 1936 Resistance of solid surfaces to wetting by water. *Ind. Engng Chem.* **28**, 988–994.

YANG, C., TARTAGLINO, U. & PERSSON, B. N. J. 2006 Influence of surface roughness on superhydrophobicity. *Phys. Rev. Lett.* **97**, 116103.

YARIV, E. & SCHNITZER, O. 2019 Speed of rolling droplets. *Phys. Rev. Fluids* **4**, 093602.

YBERT, C., BARENTIN, C., COTTIN-BIZONNE, C., JOSEPH, P. & BOCQUET, L. 2007 Achieving large slip with superhydrophobic surfaces: scaling laws for generic geometries. *Phys. Fluids* **19**, 123601.